


Ground-state phase diagram of dipolar-octupolar pyrochlores

Owen Benton 

*RIKEN Center for Emergent Matter Science (CEMS), Wako, Saitama 351-0198, Japan
and Max Planck Institute for the Physics of Complex Systems, Nöthnitzer Strasse 38, Dresden 01187, Germany*

 (Received 14 February 2020; revised 28 July 2020; accepted 3 August 2020; published 3 September 2020)

The “dipolar-octupolar” pyrochlore oxides $R_2M_2O_7$ ($R=Ce, Sm, Nd$) represent an important opportunity in the search for three-dimensional quantum spin liquid (QSL) ground states. Their low-energy physics is governed by an alluringly simple “XYZ” Hamiltonian, enabling a theoretical description with only a small number of free parameters. Meanwhile, recent experiments on Ce pyrochlores strongly suggest QSL physics. Motivated by this, we present here a complete analysis of the ground-state phase diagram of dipolar-octupolar pyrochlores. Combining cluster mean-field theory, variational arguments, and exact diagonalization we find multiple $U(1)$ QSL phases, which together occupy a large fraction of the parameter space. These results give a comprehensive picture of the ground-state physics of an important class of QSL candidates and support the possibility of a $U(1)$ QSL ground state in $Ce_2Zr_2O_7$ and $Ce_2Sn_2O_7$.

DOI: [10.1103/PhysRevB.102.104408](https://doi.org/10.1103/PhysRevB.102.104408)

I. INTRODUCTION

The pursuit of quantum spin liquid (QSL) ground states has not gone unrewarded. On the theory side, it has been realized that an enormous diversity of QSL states are possible [1,2] and several physically relevant models are now known to have QSL ground states [3–11]. In experiments, many candidate materials have been established, exhibiting spin-liquid-like properties at low temperature [12–16].

What has yet to be achieved is the combination of a material with an experimentally robust QSL state, with theoretical understanding of the microscopic interactions which give rise to that state and what kind of spin liquid they produce. Some materials studied as potential QSLs actually order at low temperature [17–19], and others are complicated by chemical or structural disorder [20–23]. Meanwhile, the relevant theoretical models are often complicated, possessing many free parameters [24–26].

“Dipolar-octupolar” (DO) pyrochlores $R_2M_2O_7$ ($R=Ce, Sm, Nd$; $M=Zr, Hf, Ti, Sn, Pb$) [27–44] constitute an opportunity in this context, with their low-energy physics being described by a simple XYZ Hamiltonian [45,46]. Out of this family, $Ce_2Sn_2O_7$ [27,28] and $Ce_2Zr_2O_7$ [29,30] have been highlighted recently as showing evidence of QSL physics. Notably, neutron scattering results for $Ce_2Zr_2O_7$ bear encouraging similarity to predictions for a $U(1)$ quantum spin liquid [30,47].

In DO pyrochlores, the magnetic rare-earth ions form a corner-sharing tetrahedral structure [Fig. 1 (inset)]. There are strong crystal electric fields (CEFs) acting on each magnetic site, resulting in a Kramers doublet at the bottom of the CEF spectrum, separated from higher states by a large gap $\Delta_{\text{CEF}} \sim 100$ K [30,37,40]. With the scale of exchange interactions being ~ 1 K [28,39], this motivates a description of the system in terms of pseudospin-1/2 operators $\tau_i^x, \tau_i^y, \tau_i^z$. The thing which sets DO pyrochlores apart from other pyrochlore oxides is the transformation properties of these operators under time-reversal and lattice symmetries [45,46].

τ_i^x and τ_i^z both transform like the component of a magnetic dipole oriented along the site’s C_3 symmetry axis, while τ_i^y transforms like a component of the magnetic octupole tensor.

Assuming nearest-neighbor interactions, symmetry constrains the Hamiltonian to take the form [45]

$$\mathcal{H} = \sum_{\langle ij \rangle} \left[\left(\sum_{\alpha=x,y,z} J_{\alpha} \tau_i^{\alpha} \tau_j^{\alpha} \right) + J_{xz} (\tau_i^x \tau_j^z + \tau_i^z \tau_j^x) \right]. \quad (1)$$

The final term in Eq. (1) can be removed by a suitably chosen global transformation $\tau^{\alpha} \rightarrow \tilde{\tau}^{\alpha}$ [45,48], reducing the problem to an XYZ Hamiltonian

$$\mathcal{H} = \sum_{\langle ij \rangle} \sum_{\alpha=x,y,z} \tilde{J}_{\alpha} \tilde{\tau}_i^{\alpha} \tilde{\tau}_j^{\alpha}. \quad (2)$$

An understanding of dipolar-octupolar pyrochlores and their potential to realize QSL ground states requires understanding of the ground-state phase diagram of Eq. (2).

Certain limits of the parameter space of Eq. (2) have been well studied, namely, the perturbative limit where one exchange parameter dominates the other two [4,47,49], the XXZ limit where two of the three exchange parameters are equal [5,50–54] and the region of parameter space without a sign problem for quantum Monte Carlo (QMC) [5,45,53–55]. However, there is no reason to expect materials

Published by the American Physical Society under the terms of the Creative Commons Attribution 4.0 International license. Further distribution of this work must maintain attribution to the author(s) and the published article’s title, journal citation, and DOI. Open access publication funded by the Max Planck Society.

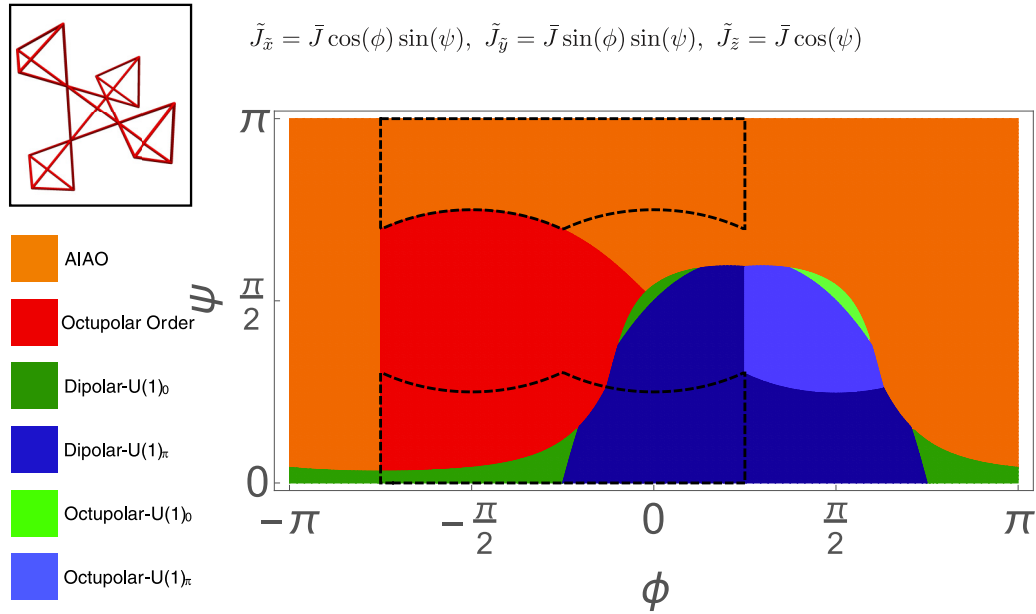


FIG. 1. Ground-state phase diagram of the XYZ model [Eq. (2)] on the pyrochlore lattice (inset), describing dipolar-octupolar pyrochlores. The three exchange parameters \tilde{J}_α are represented in terms of an overall scale \bar{J} and two angular variables ϕ, ψ [Eq. (3)]. The phase diagram features “all in/all out” (AIAO) and octupolar ordered phases, and four distinct $U(1)$ QSLs. These four QSLs are distinguished by whether the emergent electric field of the low-energy gauge theory transforms like a magnetic dipole or octupole, and by the flux penetrating elementary plaquettes in the ground state (0 or π). The phase diagram is obtained by combining cluster mean-field theory (CMFT), a cluster variational (CVAR) calculation, and exact diagonalization (ED) as described in the text. The two regions bounded by black dashed lines correspond to the subset of parameters in Eq. (5), from which the entire phase diagram can be generated using unitary transformations.

of interest to fall into one of these limits, so a global phase diagram is needed.

In this paper, we calculate the ground-state phase diagram of Eq. (2), by combining cluster mean-field theory (CMFT), a variational extension to CMFT (CVAR) [52] and exact diagonalization (ED).

Where the results can be compared with available QMC results [55], they agree well.

The final result for the phase diagram is shown in Fig. 1, with the parameter space expressed in terms of an overall scale \bar{J} which can be divided out and two angles ϕ, ψ :

$$\begin{aligned} \tilde{J}_x &= \bar{J} \cos(\phi) \sin(\psi), \tilde{J}_y = \bar{J} \sin(\phi) \sin(\psi), \\ \tilde{J}_z &= \bar{J} \cos(\psi). \end{aligned} \quad (3)$$

We find four $U(1)$ spin liquid phases, occupying a large combined portion of the parameter space, competing with an antiferromagnetic “all in/all out” (AIAO) phase and octupolar order.

The four $U(1)$ QSLs all host gapless photons and gapped fractionalized charges, and are thus realizations of emergent electromagnetism [4,6,47,49].

They are labeled dipolar/octupolar- $U(1)_{0/\pi}$ with the dipolar/octupolar label referring to whether the emergent electric field transforms like a magnetic dipole or octupole [56,57], and the $0/\pi$ subscript referring to the $U(1)$ flux penetrating elementary plaquettes in the ground state.

The remainder of this paper is devoted to explaining the calculations leading to Fig. 1, before finishing with a brief discussion of the outlook for experiments.

The paper is structured as follows. In Sec. II we describe some simple dualities which allow the whole phase diagram to be generated from calculations covering only a subregion of parameter space. In Sec. III we calculate the ground-state phase diagram using CMFT, augmented with the CVAR approach. In Sec. IV we show ED calculations on a 16-site cluster, and use these as an alternative route to calculate the ground-state phase diagram. The construction of the complete phase diagram (Fig. 1), from the combination of the calculations in the preceding sections, is then described in Sec. V. Section VI gives a summary of the results and an outlook for future work on dipolar-octupolar pyrochlores.

II. DUALITIES OF THE MODEL AND REDUCED PARAMETER SPACE

In calculating the phase diagram it is useful to note that Eq. (2) has some dualities in which the exchange parameters can be permuted by a unitary transformation acting on \mathcal{H} . Specifically,

$$\begin{aligned} \mathcal{H}(\tilde{J}_z, \tilde{J}_x, \tilde{J}_y) &= \mathcal{U}_{2\pi/3, 111} \mathcal{H}(\tilde{J}_x, \tilde{J}_y, \tilde{J}_z) \mathcal{U}_{2\pi/3, 111}^\dagger, \\ \mathcal{H}(\tilde{J}_y, \tilde{J}_x, \tilde{J}_z) &= \mathcal{U}_{\pi/2, 001} \mathcal{H}(\tilde{J}_x, \tilde{J}_y, \tilde{J}_z) \mathcal{U}_{\pi/2, 001}^\dagger, \end{aligned} \quad (4)$$

where $\mathcal{U}_{\gamma, \mathbf{v}}$ represents a global rotation by an angle γ around axis \mathbf{v} of pseudospin space (which is not the same as a rotation in the physical crystal space). Making use of these dualities means that we do not actually need to study the full parameter space of $\tilde{J}_x, \tilde{J}_y, \tilde{J}_z$, it is enough to consider a subset of parameters

$$|\tilde{J}_z| > |\tilde{J}_x|, |\tilde{J}_y|, \quad \tilde{J}_x > \tilde{J}_y, \quad (5)$$

from which we can then generate the rest of the phase diagram by applying the transformations from Eq. (4) to our results. The parameter space described by Eq. (5) is delineated by the black dashed lines in Fig. 1.

Taking \tilde{J}_z to be the strongest exchange parameter as in Eq. (5), if $\tilde{J}_z < 0$ it is clear that the ground state will simply order ferromagnetically with respect to the \tilde{z} -axis of pseudospin space. In terms of the physical magnetic moments this implies AIAO order. The more challenging problem is to discover what happens when $\tilde{J}_z > 0$.

To study this case we rewrite the Hamiltonian in terms of spin ladder operators $\tilde{\tau}_i^\pm$:

$$\mathcal{H} = \sum_{\langle ij \rangle} [\tilde{J}_z \tilde{\tau}_i^z \tilde{\tau}_j^z - \tilde{J}_\pm (\tilde{\tau}_i^+ \tilde{\tau}_j^- + \tilde{\tau}_i^- \tilde{\tau}_j^+) + \tilde{J}_{\pm\pm} (\tilde{\tau}_i^+ \tilde{\tau}_j^+ + \tilde{\tau}_i^- \tilde{\tau}_j^-)], \quad (6)$$

where $\tilde{J}_\pm = -\frac{1}{4}(\tilde{J}_x + \tilde{J}_y)$ and $\tilde{J}_{\pm\pm} = \frac{1}{4}(\tilde{J}_x - \tilde{J}_y)$. The subregion of parameter space given by Eq. (5) then becomes

$$|2(\tilde{J}_{\pm\pm} - \tilde{J}_\pm)| < \tilde{J}_z, \quad |2(\tilde{J}_{\pm\pm} + \tilde{J}_\pm)| < \tilde{J}_z, \quad \tilde{J}_{\pm\pm} > 0. \quad (7)$$

III. PHASE DIAGRAM FROM CLUSTER MEAN-FIELD THEORY

A. CMFT Calculation

To begin, we consider the phase diagram using a tetrahedral CMFT, as employed for the XXZ limit ($\tilde{J}_{\pm\pm} = 0$) in Ref. [52]. A summary of the calculation is given here, with a detailed description found in Appendix A.

To construct the CMFT we use the fact that the pyrochlore lattice can be divided into two sets of tetrahedra ‘‘A’’ and ‘‘B,’’ with all neighbors of an ‘‘A’’ tetrahedron being ‘‘B’’ tetrahedra and vice versa. We then seek to optimize a product wave function over all ‘‘A’’ tetrahedra:

$$|\psi_{\text{CMFT}}\rangle = \prod_{t \in A} |\phi_t\rangle. \quad (8)$$

The wave function $|\phi_t\rangle$ on each tetrahedron t is defined to be the ground state of a single tetrahedron Hamiltonian

$$\mathcal{H}'_t |\phi_t\rangle = \epsilon_{0,t} |\phi_t\rangle. \quad (9)$$

\mathcal{H}'_t contains the original exchange terms acting on the bonds of t as well as auxiliary fields \mathbf{h}_i on each site

$$\begin{aligned} \mathcal{H}'_t = & \sum_{(ij) \in t} [\tilde{J}_z \tilde{\tau}_i^z \tilde{\tau}_j^z - \tilde{J}_\pm (\tilde{\tau}_i^+ \tilde{\tau}_j^- + \tilde{\tau}_i^- \tilde{\tau}_j^+) + \tilde{J}_{\pm\pm} (\tilde{\tau}_i^+ \tilde{\tau}_j^+ + \tilde{\tau}_i^- \tilde{\tau}_j^-)] \\ & - \sum_{i \in t} \sum_{\alpha = \tilde{x}, \tilde{y}, \tilde{z}} h_i^\alpha \tilde{\tau}_i^\alpha. \end{aligned} \quad (10)$$

The auxiliary fields \mathbf{h}_i then serve as variational parameters for optimizing $|\psi_{\text{CMFT}}\rangle$, and a CMFT wave function can be indexed by a configuration of \mathbf{h}_i on the lattice.

There are two regimes for the optimal configuration of \mathbf{h}_i in CMFT as shown in Fig. 2. For sufficiently large, positive, values of \tilde{J}_\pm or $\tilde{J}_{\pm\pm}$ the optimal solutions have \mathbf{h}_i ordered ferromagnetically along the y -axis of pseudospin space. This implies $\langle \tilde{\tau}^y \rangle \neq 0$, and therefore octupolar order since $\tilde{\tau}^y$ transforms like a magnetic octupole [45].

In the remainder of the phase diagram there is a large, ice-like, degeneracy of disordered CMFT solutions, with

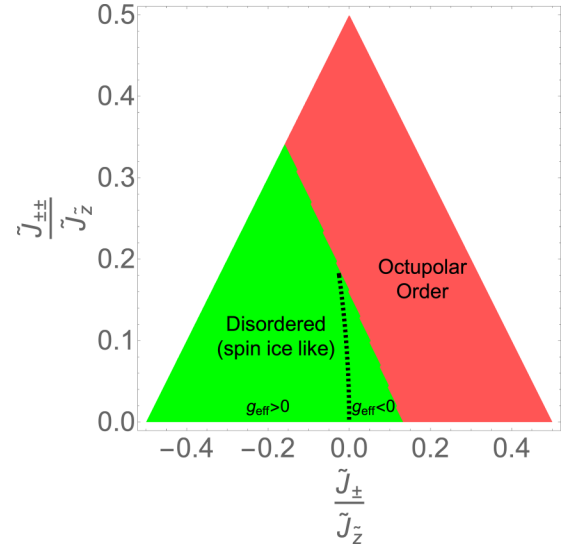


FIG. 2. CMFT and CVAR calculations of the ground-state phase diagram of \mathcal{H} [Eqs. (2) and (6)] within the region of parameter space given by Eq. (7) with $\tilde{J}_z > 0$. CMFT calculations give two regimes for the optimal configuration of the auxiliary fields \mathbf{h}_i : an ordered region where the \mathbf{h}_i point uniformly along the y axis of pseudospin space (red) and a disordered region with a large degeneracy of CMFT solutions where $\mathbf{h}_i = \sigma_i h \tilde{\mathbf{z}}_i$, with signs σ_i summing to zero on every tetrahedron (green). The CVAR calculation, which incorporates quantum tunneling between CMFT solutions, breaks the degenerate region into two, based on the sign of the effective tunneling matrix element g_{eff} . Positive (negative) values of g_{eff} lead ultimately to a π -flux (0-flux) $U(1)$ QSL ground state.

$\mathbf{h}_i = \sigma_i h \tilde{\mathbf{z}}_i$ where h is a fixed, uniform, magnitude and $\sigma_i = \pm 1$, subject to the constraint that σ_i sum to zero on every tetrahedron.

B. Cluster variational calculation

To resolve the CMFT degeneracy in the disordered regime, we follow the cluster variational (CVAR) method [52]. The calculation is described briefly here with further details given in Appendix B.

Labelling CMFT ground states according to their configuration of signs $\{\sigma\}$ we write down a generalized superposition of CMFT solutions

$$|\varphi\rangle = \sum_{\{\sigma\}} a_{\{\sigma\}} |\psi_{\text{CMFT}}(\{\sigma\})\rangle, \quad (11)$$

where $a_{\{\sigma\}}$ are unknown coefficients. We then seek to optimize the new variational energy

$$E_{\text{var}} = \frac{\langle \varphi | \mathcal{H} | \varphi \rangle}{\langle \varphi | \varphi \rangle}. \quad (12)$$

Equation (12) can be expanded in terms of the overlap between distinct CMFT wave functions, in a similar spirit to the derivation of dimer models from an expansion in the overlap between singlet coverings of a lattice [59]. This generates an effective Hamiltonian in the space of CMFT solutions, where the leading term is a six-site ring exchange which flips the values of σ_i on hexagonal plaquettes where σ alternates in sign around the plaquette, with matrix element g_{eff} .

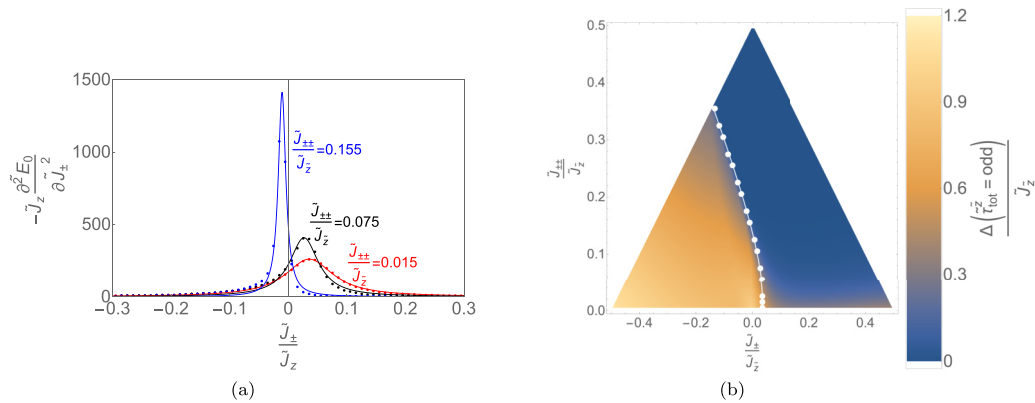


FIG. 3. ED calculations of the ground-state phase diagram of \mathcal{H} [Eqs. (2) and (6)] within the region of parameter space given by Eq. (7) with $\tilde{J}_z > 0$. (a) Second derivative of the ground-state energy in ED on a 16-site cubic cluster with respect to \tilde{J}_\pm for various values of $\tilde{J}_{\pm\pm}/\tilde{J}_z$. The peaks indicate a qualitative change in the ground state [58], associated with the transition to long-range order. (b) Color plot of the gap to excitations with odd total $\tilde{\tau}^z$ within 16-site ED. The white line indicates the position of peaks in the second derivative of the ground-state energy, examples of which are plotted in (a). The gap collapses rapidly upon crossing the white line, supporting the conclusion that this line corresponds to a transition to long-range order breaking π -rotation symmetry around the \tilde{z} -axis in the thermodynamic limit.

This Hamiltonian has already been studied using quantum Monte Carlo [47,49]. It can have two different QSL ground states depending on the sign of g_{eff} . Both are $U(1)$ QSLs with gapped, bosonic, charges and gapless photons. The two ground states are distinguished by the $U(1)$ flux threading elementary plaquettes in the ground state. This background flux vanishes for $g_{\text{eff}} < 0$ [$U(1)_0$] but is equal to π on every plaquette for $g_{\text{eff}} > 0$ [$U(1)_\pi$]. The value of g_{eff} can be extracted from the CMFT calculation for all values of exchange parameters (see Appendix B), and by this means the degenerate region within CMFT can be divided into two ground-state QSL phases [$U(1)_0$ and $U(1)_\pi$] depending on the sign of g_{eff} . The boundary between regions with different signs of g_{eff} is shown in Fig. 2. This constitutes our estimate of the boundary between 0-flux and π -flux QSLs.

IV. EXACT DIAGONALIZATION

We now turn to ED calculations on a 16-site cubic cluster with periodic boundaries, to obtain alternative estimates of the phase boundaries.

A. Boundary of octupolar ordered phase

Figure 3(a) shows the second derivative of the ground-state energy on this cluster with respect to \tilde{J}_\pm , at various fixed values of $\tilde{J}_{\pm\pm}/\tilde{J}_z$. This second derivative exhibits a peak as \tilde{J}_\pm is swept, indicating a qualitative change in the ground state [58].

Figure 3(b), shows the position of these peaks as a function of $\tilde{J}_\pm/\tilde{J}_z$ and $\tilde{J}_{\pm\pm}/\tilde{J}_z$, laid over a color plot of the gap to excitations with odd total $\tilde{\tau}^z$. The parity $p = (-1)^{\sum_i \tilde{\tau}_i^z}$ is conserved by \mathcal{H} , with the ground state always having $p = 1$. The line of peaks in the second derivative of the ground-state energy coincides with a rapid decrease of the gap to $p = -1$ excitations. This suggests the formation of a twofold degenerate ground state in the thermodynamic limit, breaking π rotation symmetry around the \tilde{z} axis, consistent with the octupolar order identified in CMFT. We thus interpret the

peaks in the second derivative of the ground-state energy as indicative of a transition to octupolar order.

B. Boundary between QSLs

It is not easy to cleanly distinguish between the two QSL phases, QSL_0 , and QSL_π using ED on a small cluster. However, some insight into how to identify the phase boundary can be gained by considering how this transition occurs in the perturbative limit and in the CVAR approach.

From the perspective of both perturbation theory and CVAR, the transition from QSL_0 to QSL_π occurs when the leading tunneling matrix element g_{eff} between ice-like states changes sign. At the point where g_{eff} vanishes, tunneling is restricted to higher-order processes and will therefore be suppressed, leading to a near restoration of the degeneracy of ice-like states.

Returning to ED, this suggests that the transition from QSL_0 to QSL_π will be accompanied by a simultaneous collapse of many excited states, in the sector with even total $\tilde{\tau}^z$, to near-zero energy. Such a collapse is indeed observed in the ED data, as shown in Fig. 4(a). The position of this collective minimum in the gaps within the even sector constitutes the ED estimate of the phase boundary between the two QSLs. The phase boundary thus obtained is compared to that from CVAR in Fig. 4(b), with the two estimates agreeing closely.

C. Combining information from CMFT/CVAR and ED

Combining the information from CMFT/CVAR and ED gives the phase diagram shown in Fig. 5.

For $\tilde{J}_\pm < 0$ the CMFT and ED estimates of the octupolar phase boundary agree closely. For $\tilde{J}_\pm > 0$ the ED estimates a larger region of octupolar order (and hence a smaller QSL region) than does the CMFT approach.

For $\tilde{J}_\pm > 0$ the model has no sign problem from the perspective of QMC, and in this regime we can compare to previous QMC studies. Several previous QMC studies of the case $\tilde{J}_{\pm\pm} = 0$ have observed the transition from QSL_0 to the

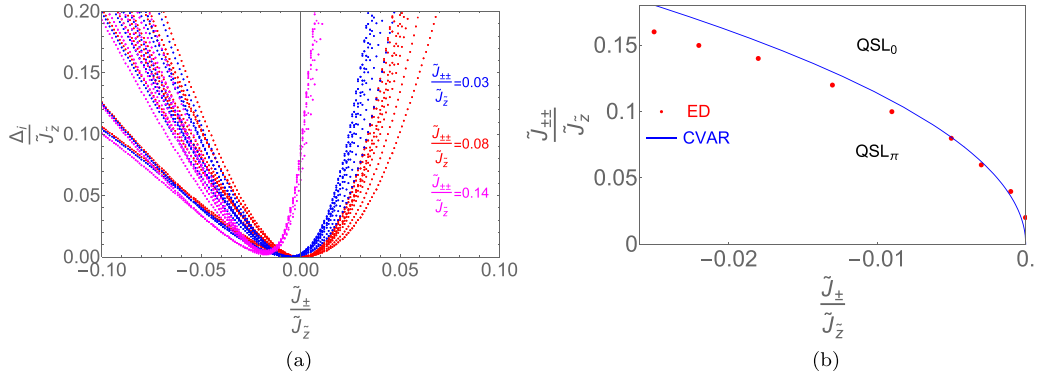


FIG. 4. Estimate of the phase boundary between the quantum spin liquids QSL_0 and QSL_π , within ED. (a) Collapse of gaps to lowest excited states in the sector with even total $\tilde{\tau}^z$, within 16-site ED. The gaps are plotted as a function of $\tilde{J}_\pm/\tilde{J}_z$ for three different values of $\tilde{J}_{\pm\pm}/\tilde{J}_z$. For a given value of $\tilde{J}_{\pm\pm}/\tilde{J}_z$ the gaps come close to zero around the same point, which we take as an indication of the suppression of tunneling within the low-energy manifold of states. This corresponds with expectations from perturbation theory and CVAR calculations for the transition between QSL_0 and QSL_π , which happens when the leading tunneling term between ice-like states changes sign. (b) The position of the collective minima in the gaps in the even sector as a function of exchange parameters, which serves as the ED estimate of the boundary between QSLs (points). This is compared to the estimate of the same phase boundary from CVAR (solid line).

ordered phase as \tilde{J}_\pm is increased [5,53–55]. A recent QMC study by Huang *et al.* [55] studied the behavior of this phase boundary as a function of $\tilde{J}_{\pm\pm}$. Comparison to these results can be used to adjudicate between ED and CVAR where they disagree. The ED calculation gives closer agreement with the QMC results from [55] than CMFT/CVAR does, and therefore we will take the ED calculation as our estimate of the boundary of the octupolar phase.

The estimates of the boundary between the two QSL phases agree closely between CVAR and ED, as shown in Fig. 4(b). There is, however, some difference between the two

estimates at larger negative values of \tilde{J}_\pm . For the purpose of Fig. 5 we use the boundary from CVAR because it gives a more direct prediction of the transition between the two states in the thermodynamic limit, as opposed to the more indirect inference from the behavior of gaps in ED.

V. CONSTRUCTION OF COMPLETE PHASE DIAGRAM

The phase diagram in Fig. 5 can then be extended to the full parameter space using the duality relations [Eq. (4)].

In doing this, we must take into account how the duality transformations act on the ground states. For example, the octupolar ordered phase with $\langle \tilde{\tau}_i^y \rangle \neq 0$ becomes an AIAO phase when acted on by a transformation which swaps the \tilde{y} -axis with the \tilde{x} -axis or \tilde{z} -axis. On the other hand, transformations which swap only the \tilde{x} -axis and \tilde{z} -axis, do not change the classification of the ground-state phase because $\tilde{\tau}_i^x$ and $\tilde{\tau}_i^z$ transform equivalently under point-group and time-reversal symmetries.

Similar considerations allow us to distinguish four different kinds of $U(1)$ QSL, generated from the two in the phase diagram of Fig. 5. In the 0-flux and π -flux QSLs in Fig. 5 the emergent electric field of the QSL $E_i \sim \tilde{\tau}_i^z$ [4,50] and therefore transforms like a magnetic dipole. If we act a transformation that swaps the \tilde{z} -axis and \tilde{y} -axes, then $E_i \sim \tilde{\tau}_i^y$ and transforms like an octupole. We should therefore not only distinguish $U(1)$ QSLs by the flux but by the dipolar or octupolar character of the emergent electric field, giving four distinct QSLs on the complete phase diagram [56,57].

Applying these arguments to the parameter space covered in Fig. 5, and to the case of $\tilde{J}_z < 0$, allows us to generate the full phase diagram, shown using spherical coordinates [Eq. (3)] in Fig. 1.

VI. SUMMARY AND OUTLOOK

We thus established a phase diagram for the generic, symmetry allowed, nearest-neighbor exchange Hamiltonian describing dipolar-octupolar (DO) pyrochlores $\text{R}_2\text{M}_2\text{O}_7$ ($\text{R}=\text{Ce}$,

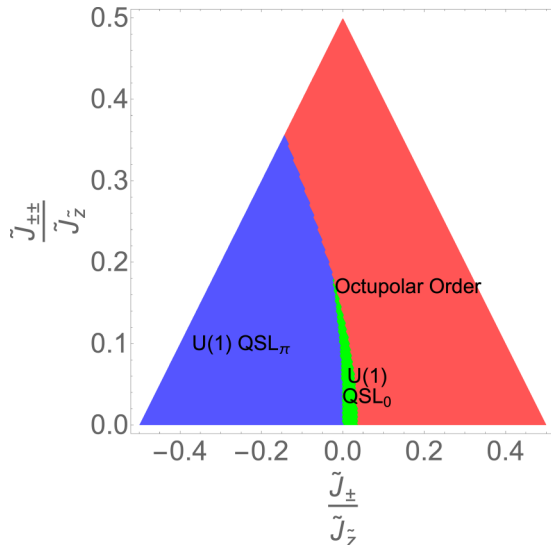


FIG. 5. Ground-state phase diagram of \mathcal{H} [Eqs. (2) and (6)], in the parameter region (7) with $\tilde{J}_z > 0$, obtained from combining CMFT, CVAR, and ED calculations. This region of parameter space corresponds to the lower region bounded by dashed lines in Fig. 1. The full phase diagram in Fig. 1 can be generated by applying the dualities described in Sec. II to this region and to the upper region bounded by dashed lines in Fig. 1 which has all-in-all-out order throughout.

Sm, Nd). The picture we arrive at is an encouraging one for the realization of QSL states. There are four distinct $U(1)$ QSLs on the phase diagram of the generic nearest neighbor model, and between them they occupy $\sim 19\%$ of the available parameter space.

Amongst materials, $\text{Ce}_2\text{Zr}_2\text{O}_7$ [29,30], $\text{Ce}_2\text{Sn}_2\text{O}_7$ [27,28], and $\text{Sm}_2\text{Zr}_2\text{O}_7$ [35] stand out as lacking low-temperature order. The Ce pyrochlores in particular seem promising with recent neutron scattering results on $\text{Ce}_2\text{Zr}_2\text{O}_7$ bearing similarity to predictions for emergent photons [30]. Low-energy correlations in $\text{Ce}_2\text{Sn}_2\text{O}_7$ seem to be dominantly octupolar in nature [28], which would be consistent with either of the two octupolar spin liquids on the phase diagram (Fig. 1).

It will be important to establish estimates of the exchange parameters of $\text{Ce}_2\text{Zr}_2\text{O}_7$ and $\text{Ce}_2\text{Sn}_2\text{O}_7$, combining information from inelastic neutron scattering with fits to thermodynamic data. Mean-field calculations in Ref. [28] give an initial estimate for $\text{Ce}_2\text{Sn}_2\text{O}_7$ of $J_y = 0.48$ K, $J_z = 0.03$ K, while setting J_x and J_{xz} to zero, in the basis of Eq. (1). This would place $\text{Ce}_2\text{Sn}_2\text{O}_7$ in the Octupolar- $U(1)_\pi$ region of the phase diagram. It would be useful to refine this estimate with all parameters allowed to be finite, and using calculations beyond mean-field theory.

If refined parametrizations place $\text{Ce}_2\text{Zr}_2\text{O}_7$ and $\text{Ce}_2\text{Sn}_2\text{O}_7$ within the QSL regimes of Fig. 1, then this will be a strong indication that they are indeed $U(1)$ QSLs, and the parameterized model will provide a platform for further theoretical study. Understanding the effects of disorder of the crystal structure is also likely to be crucial, particularly in regard to the possible substitution of magnetic Ce^{3+} with nonmagnetic Ce^{4+} [30].

For those DO pyrochlores that are known to possess magnetic order at low temperature, the spin liquid phases may also manifest at finite temperature, as suggested recently in $\text{Nd}_2\text{Zr}_2\text{O}_7$ [60]. In such cases it may even be possible to tune into the $T = 0$ QSL phase using chemical or physical pressure, giving another avenue to realize these exotic states of matter.

Note added. Recently, the author became aware of a recent paper by Patri *et al.* [61], which also presents calculations of the ground-state phase diagram of DO pyrochlores.

ACKNOWLEDGMENTS

The author acknowledges useful discussions with Andrea Bianchi, Jonathan Gaudet, Bruce Gaulin, Ludovic Jaubert, Bella Lake, Kate Ross, Nic Shannon, Romain Sibille, Rajiv Singh, Evan Smith, Jianhui Xu, and Danielle Yahne. The author also thanks Paul McClarty for comments on the draft manuscript.

APPENDIX A: CMFT SOLUTIONS IN THE ICE-LIKE REGIME

The CMFT proceeds by optimizing variational wave functions of the form

$$|\psi_{\text{CMFT}}(\{\mathbf{h}_i\})\rangle = \prod_{t \in A} |\phi_t(\{\mathbf{h}_{i \in t}\})\rangle, \quad (\text{A1})$$

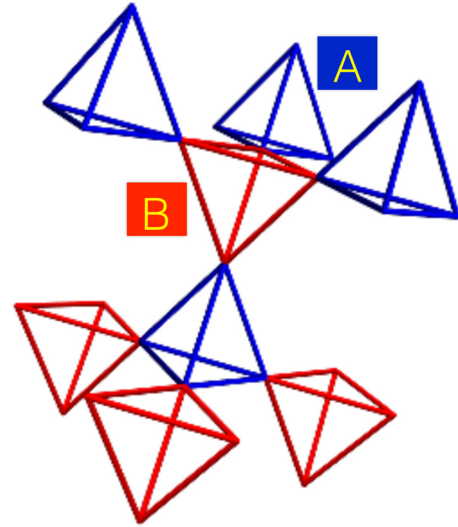


FIG. 6. The pyrochlore lattice with “A” and “B” tetrahedra highlighted in red and blue, respectively.

where the product is over all “A” tetrahedra (Fig. 6), $\{\mathbf{h}_i\}$ is the configuration of auxiliary fields defined on each site and the single tetrahedron wave functions $|\phi_t\rangle$ depend only on the fields on sites belonging to tetrahedron t . The auxiliary fields \mathbf{h}_i are variational parameters for optimizing the CMFT energy

$$E_{\text{CMFT}} = \langle \psi_{\text{CMFT}} | \mathcal{H} | \psi_{\text{CMFT}} \rangle. \quad (\text{A2})$$

The wave functions $|\phi_t(\{\mathbf{h}_{i \in t}\})\rangle$ are taken to be eigenstates of a single tetrahedron Hamiltonian \mathcal{H}'_t

$$\mathcal{H}'_t = \sum_{(ij) \in t} \sum_{\alpha = \bar{x}, y, z} \tilde{J}_{\alpha} \tilde{\tau}_i^{\alpha} \tilde{\tau}_j^{\alpha} - \sum_{i \in t} \sum_{\alpha = \bar{x}, y, z} h_i^{\alpha} \tilde{\tau}_i^{\alpha} \quad (\text{A3})$$

$$\mathcal{H}'_t |\phi_t(\{\mathbf{h}_{i \in t}\})\rangle = \epsilon_{0,t} |\phi_t(\{\mathbf{h}_{i \in t}\})\rangle. \quad (\text{A4})$$

E_{CMFT} is then

$$E_{\text{CMFT}} = \sum_{t \in A} \epsilon_{0,t} + \sum_i \sum_{\alpha = \bar{x}, y, z} h_i^{\alpha} \langle \tilde{\tau}_i^{\alpha} \rangle + \sum_{(ij) \in B} \sum_{\alpha = \bar{x}, y, z} \tilde{J}_{\alpha} \langle \tilde{\tau}_i^{\alpha} \rangle \langle \tilde{\tau}_j^{\alpha} \rangle, \quad (\text{A5})$$

where the final term in Eq. (A5) sums over bonds belonging to “B” tetrahedra and accounts for the interactions on those tetrahedra.

There is a large region of the phase diagram (Fig. 2 of the main text) in which the optimal solutions for \mathbf{h}_i take the form

$$h_i^{\bar{x}} = h_i^{\bar{y}} = 0, h_z^{\bar{z}} = \sigma_i h, \quad \sigma_i = \pm 1. \quad (\text{A6})$$

Correspondingly, the expectation values of the spin components are

$$\langle \tilde{\tau}_i^{\bar{x}} \rangle = \langle \tilde{\tau}_i^{\bar{y}} \rangle = 0, \quad \langle \tilde{\tau}_i^{\bar{z}} \rangle = \sigma_i s, \quad (\text{A7})$$

with h and s being uniform across the system, and fixed by the energy optimization for a given parameter set.

With this form for the auxiliary fields, the mean-field energy [Eq. (A5)] becomes

$$E_{\text{CMFT}} = \sum_{t \in A} \epsilon_{0,t} + Nhs + \tilde{J}_z s^2 \sum_{(ij)_B} \sigma_i \sigma_j. \quad (\text{A8})$$

Any arrangement of signs σ_i such that

$$\sum_{i \in t} \sigma_i = 0 \quad \forall \text{ tetrahedra } t \quad (\text{A9})$$

gives rise to the same value of $\epsilon_{0,t}$, as can be inferred from the symmetries of the original Hamiltonian. The remaining terms in Eq. (A8) are also the same for all configurations obeying Eq. (A9). Thus we have a large degeneracy of mean-field solutions in this regime.

Each arrangement of signs σ_i obeying Eq. (A9) defines a CMFT wave function [via Eqs. (A1), (A4), and (A6)] which we will denote with $|\psi_{\text{CMFT}}(\{\sigma\})\rangle$. Explicitly, the form of single tetrahedron wave functions $|\phi_t(\{\sigma_{i \in t}\})\rangle$ (denoted simply as $|\sigma_0 \sigma_1 \sigma_2 \sigma_3\rangle$) relates to the configuration of signs on t in the following way, written in the basis diagonalizing $\tilde{\tau}_i^z$:

$$\begin{aligned} |++--\rangle &= \sqrt{1 - \mu^2 - \nu^2 - \rho^2} |\uparrow\uparrow\downarrow\downarrow\rangle \\ &+ \frac{\mu}{2} (|\uparrow\downarrow\uparrow\downarrow\rangle + |\uparrow\downarrow\downarrow\uparrow\rangle \\ &+ |\downarrow\uparrow\uparrow\downarrow\rangle + |\downarrow\uparrow\downarrow\uparrow\rangle) \\ &+ \nu |\downarrow\downarrow\uparrow\uparrow\rangle + \frac{\rho}{\sqrt{2}} (|\uparrow\uparrow\uparrow\uparrow\rangle + |\downarrow\downarrow\downarrow\downarrow\rangle) \end{aligned}$$

$$\begin{aligned} |+-+-\rangle &= \sqrt{1 - \mu^2 - \nu^2 - \rho^2} |\uparrow\downarrow\uparrow\downarrow\rangle \\ &+ \frac{\mu}{2} (|\uparrow\uparrow\downarrow\downarrow\rangle + |\uparrow\downarrow\downarrow\uparrow\rangle \\ &+ |\downarrow\uparrow\uparrow\downarrow\rangle + |\downarrow\uparrow\downarrow\uparrow\rangle) \\ &+ \nu |\downarrow\downarrow\uparrow\uparrow\rangle + \frac{\rho}{\sqrt{2}} (|\uparrow\uparrow\uparrow\uparrow\rangle + |\downarrow\downarrow\downarrow\downarrow\rangle) \end{aligned}$$

$$\begin{aligned} |+---\rangle &= \sqrt{1 - \mu^2 - \nu^2 - \rho^2} |\uparrow\downarrow\downarrow\uparrow\rangle \\ &+ \frac{\mu}{2} (|\uparrow\uparrow\downarrow\downarrow\rangle + |\uparrow\downarrow\downarrow\uparrow\rangle \\ &+ |\downarrow\uparrow\uparrow\downarrow\rangle + |\downarrow\uparrow\downarrow\uparrow\rangle) \\ &+ \nu |\downarrow\downarrow\uparrow\uparrow\rangle + \frac{\rho}{\sqrt{2}} (|\uparrow\uparrow\uparrow\uparrow\rangle + |\downarrow\downarrow\downarrow\downarrow\rangle) \end{aligned}$$

$$\begin{aligned} |--++\rangle &= \sqrt{1 - \mu^2 - \nu^2 - \rho^2} |\downarrow\downarrow\uparrow\uparrow\rangle \\ &+ \frac{\mu}{2} (|\uparrow\downarrow\uparrow\downarrow\rangle + |\uparrow\downarrow\downarrow\uparrow\rangle \\ &+ |\downarrow\uparrow\uparrow\downarrow\rangle + |\downarrow\uparrow\downarrow\uparrow\rangle) \\ &+ \nu |\uparrow\uparrow\downarrow\downarrow\rangle + \frac{\rho}{\sqrt{2}} (|\uparrow\uparrow\uparrow\uparrow\rangle + |\downarrow\downarrow\downarrow\downarrow\rangle) \end{aligned}$$

$$\begin{aligned} |-+-+\rangle &= \sqrt{1 - \mu^2 - \nu^2 - \rho^2} |\downarrow\uparrow\downarrow\uparrow\rangle \\ &+ \frac{\mu}{2} (|\uparrow\uparrow\downarrow\downarrow\rangle + |\uparrow\downarrow\downarrow\uparrow\rangle \\ &+ |\downarrow\uparrow\uparrow\downarrow\rangle + |\downarrow\uparrow\downarrow\uparrow\rangle) \\ &+ \nu |\uparrow\downarrow\uparrow\downarrow\rangle + \frac{\rho}{\sqrt{2}} (|\uparrow\uparrow\uparrow\uparrow\rangle + |\downarrow\downarrow\downarrow\downarrow\rangle) \end{aligned}$$

$$|-++-\rangle = \sqrt{1 - \mu^2 - \nu^2 - \rho^2} |\downarrow\uparrow\uparrow\downarrow\rangle$$

$$\begin{aligned} &+ \frac{\mu}{2} (|\uparrow\uparrow\downarrow\downarrow\rangle + |\uparrow\downarrow\uparrow\downarrow\rangle \\ &+ |\downarrow\uparrow\downarrow\uparrow\rangle + |\downarrow\downarrow\uparrow\uparrow\rangle) \\ &+ \nu |\uparrow\downarrow\uparrow\downarrow\rangle + \frac{\rho}{\sqrt{2}} (|\uparrow\uparrow\uparrow\uparrow\rangle + |\downarrow\downarrow\downarrow\downarrow\rangle). \end{aligned} \quad (\text{A10})$$

The parameters μ , ν , and ρ can always be chosen to be real. This choice, combined with the choice to define the first term on the right-hand side of each line of Eq. (A10) to be positive, removes any phase ambiguity in the CMFT wave functions. μ , ν , and ρ vary as a function of the exchange parameters $\tilde{J}_{\tilde{\alpha}}$ and are plotted in Fig. 7.

APPENDIX B: DETAILS OF CVAR CALCULATION

The goal of the CVAR calculation is to resolve the degeneracy of the CMFT solutions by considering a new trial wave function which is a superposition of the CMFT solutions

$$|\varphi\rangle = \sum_{\{\sigma\}} a_{\{\sigma\}} |\psi_{\text{CMFT}}(\{\sigma\})\rangle, \quad (\text{B1})$$

where $a_{\{\sigma\}}$ are, *a priori* unknown, complex, coefficients.

We then seek to optimize the variational energy

$$\begin{aligned} E_{\text{var}} &= \frac{\langle \varphi | \mathcal{H} | \varphi \rangle}{\langle \varphi | \varphi \rangle} = \frac{\sum_{\{\sigma\}\{\sigma'\}} a_{\{\sigma'\}}^* a_{\{\sigma\}} X_{\{\sigma'\}\{\sigma\}}}{\sum_{\{\sigma\}\{\sigma'\}} a_{\{\sigma'\}}^* a_{\{\sigma\}} O_{\{\sigma'\}\{\sigma\}}} \\ &\equiv \frac{\mathbf{a}^\dagger \cdot \mathbf{X} \cdot \mathbf{a}}{\mathbf{a}^\dagger \cdot \mathbf{O} \cdot \mathbf{a}}, \end{aligned} \quad (\text{B2})$$

where \mathbf{X} is a matrix containing the Hamiltonian matrix elements between different CMFT wave functions and \mathbf{O} contains the overlaps (the CMFT wave functions are not generally orthogonal to one another)

$$X_{\{\sigma'\}\{\sigma\}} = \langle \psi_{\text{CMFT}}(\{\sigma'\}) | \mathcal{H} | \psi_{\text{CMFT}}(\{\sigma\}) \rangle, \quad (\text{B3})$$

$$O_{\{\sigma'\}\{\sigma\}} = \langle \psi_{\text{CMFT}}(\{\sigma'\}) | \psi_{\text{CMFT}}(\{\sigma\}) \rangle. \quad (\text{B4})$$

It is then useful to define a new matrix \mathbf{X}' with vanishing diagonal elements

$$\mathbf{X}' = \mathbf{X} - E_{\text{CMFT}} \mathbf{O} \quad (\text{B5})$$

such that

$$E_{\text{var}} = E_{\text{CMFT}} + \frac{\mathbf{a}^\dagger \cdot \mathbf{X}' \cdot \mathbf{a}}{\mathbf{a}^\dagger \cdot \mathbf{O} \cdot \mathbf{a}}. \quad (\text{B6})$$

We then relate the vector of coefficients \mathbf{a} , to a new normalized vector \mathbf{b} via

$$\mathbf{a} = \mathbf{O}^{-1/2} \cdot \mathbf{b}, \quad (\text{B7})$$

$$\mathbf{b}^\dagger \cdot \mathbf{b} = 1. \quad (\text{B8})$$

The variational energy is then

$$E_{\text{var}} = E_{\text{CMFT}} + \mathbf{b}^\dagger \cdot \mathbf{H}_{\text{eff}} \cdot \mathbf{b}, \quad (\text{B9})$$

where

$$\mathbf{H}_{\text{eff}} = \mathbf{O}^{-1/2} \cdot \mathbf{X}' \cdot \mathbf{O}^{-1/2}. \quad (\text{B10})$$

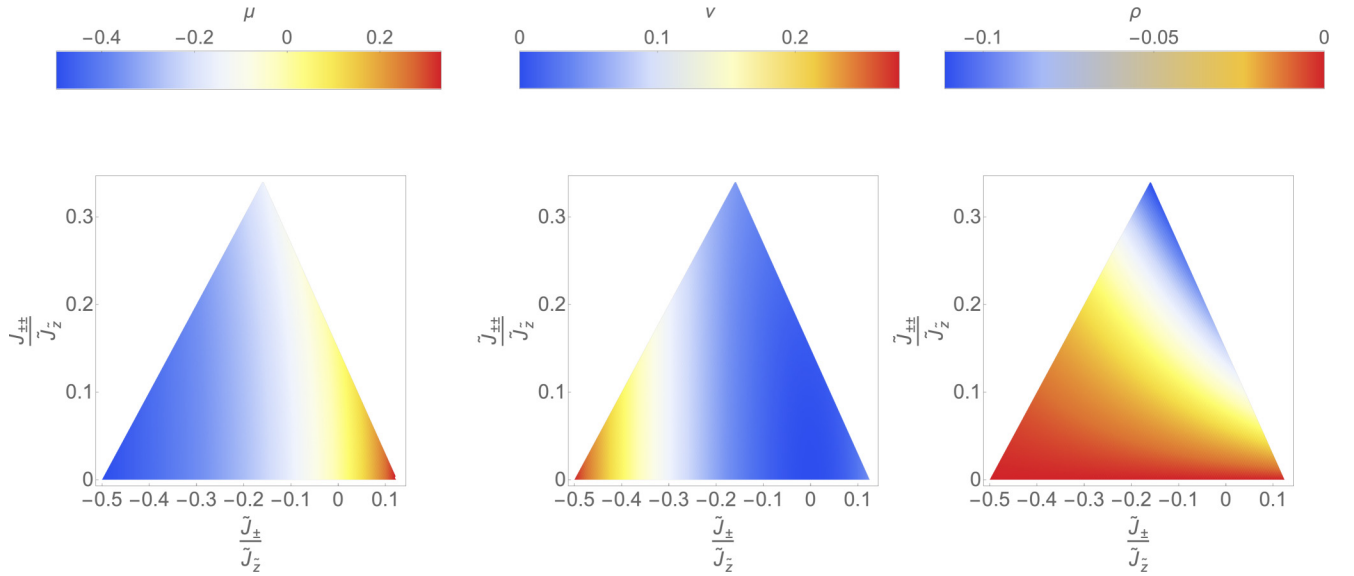


FIG. 7. Parameters μ , ν , and ρ which enter the single tetrahedron wave functions [Eq. (A10)], plotted as a function of the exchange parameters in the region where the CMFT solutions have an ice-like degeneracy.

The optimal superposition of CMFT solutions is then given by the ground state of \mathbf{H}_{eff} and Eq. (B7).

We then expand \mathbf{H}_{eff} in terms of two overlap parameters o_2 and o_4 , which can be defined from the wave functions in Eqs. (A10):

$$o_2 = \langle + + - - | + - + - \rangle = \frac{\mu^2}{2} + \rho^2 + \mu(\nu + \sqrt{1 - \mu^2 - \nu^2 - \rho^2}), \quad (\text{B11})$$

$$o_4 = \langle + + - - | + - + - \rangle = \mu^2 + \rho^2 + 2\nu\sqrt{1 - \mu^2 - \nu^2 - \rho^2}. \quad (\text{B12})$$

These two quantities are treated as small parameters for the purposes of the expansion and indeed they are small through most of the relevant parameter space, as shown in Fig. 8.

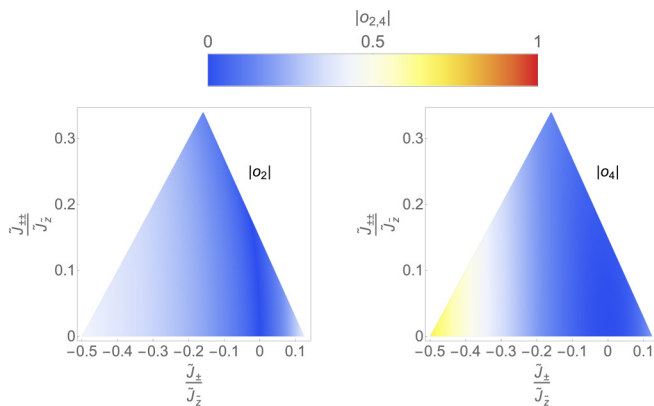


FIG. 8. Magnitudes of the single tetrahedron overlap parameters o_2 and o_4 . These function as the small parameters for the expansion of the CVAR energy.

To expand Eq. (B10) we note that all the diagonal elements of \mathbf{O} are unity, and the leading off diagonal elements $\sim (o_2)^3$ (coming from the process illustrated in Fig. 9) so we can write

$$\mathbf{O}^{-1/2} = (1 + \mathbf{O}')^{-1/2} \approx 1 - \frac{1}{2}\mathbf{O}'. \quad (\text{B13})$$

The first two terms of the expansion of \mathbf{H}_{eff} are then

$$\mathbf{H}_{\text{eff}} \approx \mathbf{X}' - \frac{1}{2}(\mathbf{O}' \cdot \mathbf{X}' + \mathbf{X}' \cdot \mathbf{O}'). \quad (\text{B14})$$

The leading elements in \mathbf{X}' are $\sim (o_2)^2$ (again, from the process in Fig. 9) and the leading elements in $\mathbf{O}' \cdot \mathbf{X}'$ are $\sim (o_2)^5$ and so we henceforth drop the second term.

We then need to evaluate the leading matrix elements in \mathbf{X}' which connect configurations of σ_i which differ on a single hexagonal plaquette as shown in Fig. 9. The matrix element to a flip a hexagon is g_{eff} . The sign of g_{eff} determines whether the ground state should be a 0 or π flux QSL, with

$$g_{\text{eff}} < 0 \Rightarrow \text{U}(1)\text{QSL}_0, \quad (\text{B15})$$

$$g_{\text{eff}} > 0 \Rightarrow \text{U}(1)\text{QSL}_\pi, \quad (\text{B16})$$

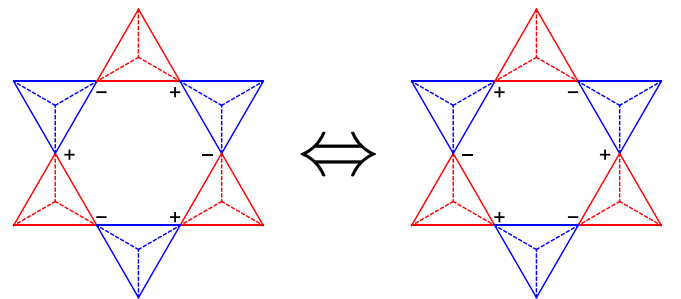


FIG. 9. Processes which flip a six-site loop of alternating sign variables σ_i provide the leading matrix elements in \mathbf{X}' , \mathbf{O}' , and \mathbf{H}_{eff} [Eq. (B10)] [52].

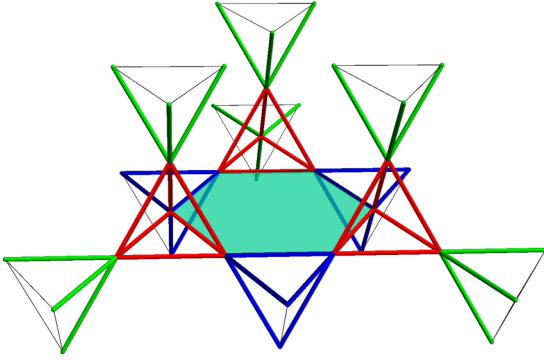


FIG. 10. Contributions to g_{eff} . The matrix element between two configurations which differ by flipping the central hexagon has three distinct nonvanishing contributions: from the “A” tetrahedra highlighted in red, from the “B;” bonds in blue which connect to the interior of the hexagon and from the “B;” bonds in green which connect to the exterior of the “A” tetrahedra belonging to the hexagon. The contribution from bonds drawn with narrow black lines vanishes.

as may be inferred from prior quantum Monte Carlo studies of the six-site ring exchange Hamiltonian [49] and from a unitary transformation which relates the sign-problem free case ($g_{\text{eff}} < 0$) to the frustrated case ($g_{\text{eff}} > 0$) [4].

Quite generally the matrix element of \mathbf{X}' between two CMFT wave functions can be written as

$$X'_{\{\sigma'\}|\{\sigma\}} = \sum_{t \in A} (\langle \psi_{\text{CMFT}}(\{\sigma'\}) | \mathcal{H}_t | \psi_{\text{CMFT}}(\{\sigma\}) \rangle - \epsilon_A \mathcal{O}_{\{\sigma'\}|\{\sigma\}}) + \sum_{(ij) \in B} \tilde{J}_z (\langle \psi_{\text{CMFT}}(\{\sigma'\}) | \tilde{\tau}_i^z \tilde{\tau}_j^z | \psi_{\text{CMFT}}(\{\sigma\}) \rangle - s^2 \sigma_i \sigma_j \mathcal{O}_{\{\sigma'\}|\{\sigma\}}), \quad (\text{B17})$$

where the first sum is over “A” tetrahedra and the second is over bonds belonging to “B” tetrahedra. \mathcal{H}_t is the original exchange Hamiltonian on tetrahedron t [distinct from \mathcal{H}'_t in Eq. (A3)] and

$$\begin{aligned} \epsilon_A &= \langle ++-- | \mathcal{H}_t | ++-- \rangle \\ &= \tilde{J}_z \left(-\frac{1}{2} + 2\rho^2 \right) \\ &\quad + 2\sqrt{2}\tilde{J}_{\pm\pm}\rho(2\mu + v + \sqrt{1 - \mu^2 - v^2 - \rho^2}) \\ &\quad - 2\tilde{J}_{\pm}\mu[\mu + 2(v + \sqrt{1 - \mu^2 - v^2 - \rho^2})]. \end{aligned} \quad (\text{B18})$$

The contribution of any “A” tetrahedron which does not change configurations between $\{\sigma'\}$ and $\{\sigma\}$ to Eq. (B17) vanishes. Similarly, the contribution of any “B” bond connecting two unchanged “A” tetrahedra vanishes.

There are three kinds of nonvanishing contribution to the matrix element to flip a hexagon. Firstly, the three “A” tetrahedra belonging to the flipped hexagon (highlighted in red in Fig. 10) contribute

$$g_A = (o_2)^2(\eta_2 - o_2\epsilon_A), \quad (\text{B19})$$

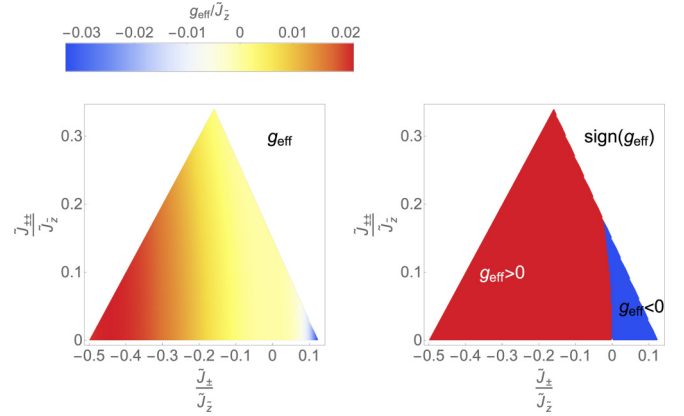


FIG. 11. Tunnelling matrix element g_{eff} , calculated using Eq. (B24), and the numerically determined CMFT wave functions, plotted over the region of parameter space where the CMFT solutions are highly degenerate. The sign of g_{eff} , shown in the second panel, determines whether a 0-flux or π -flux $U(1)$ QSL phase is predicted.

where

$$\begin{aligned} \eta_2 &= \langle ++-- | \mathcal{H}_t | ++-- \rangle \\ &= -\frac{1}{4}\tilde{J}_z \left[\mu^2 - 6\rho^2 + 2\mu(v + \sqrt{1 - \mu^2 - v^2 - \rho^2}) \right] \\ &\quad + 2\sqrt{2}\tilde{J}_{\pm\pm}\rho(2\mu + v + \sqrt{1 - \mu^2 - v^2 - \rho^2}) \\ &\quad - \tilde{J}_{\pm} [1 - \rho^2 + 2(\mu + v)(\mu + \sqrt{1 - \mu^2 - v^2 - \rho^2})]. \end{aligned} \quad (\text{B20})$$

Second, there are contributions from “B” bonds connecting to the interior of the flipped hexagon (highlighted in blue in Fig. 10)

$$g_{B1,ij} = -\tilde{J}_z s^2 \sigma_i \sigma_j (o_2)^3. \quad (\text{B21})$$

Finally, there are contributions from “B” bonds connecting to the exterior of the “A” tetrahedra on the flipped hexagon (highlighted in green in Fig. 10)

$$g_{B2,ij} = \tilde{J}_z s(\zeta - s)\sigma_i \sigma_j (o_2)^3, \quad (\text{B22})$$

where

$$\begin{aligned} \zeta &= \frac{\langle ++-- | \tilde{\tau}_0^z | ++-- \rangle}{o_2} \\ &= \frac{\mu(-v + \sqrt{1 - \mu^2 - v^2 - \rho^2})}{\mu^2 + 2\rho^2 + 2\mu(v + \sqrt{1 - \mu^2 - v^2 - \rho^2})}. \end{aligned} \quad (\text{B23})$$

Summing these contributions and accounting for the fact that σ_i must alternate around the hexagon and must obey Eq. (A9) everywhere, we arrive at the matrix element

$$g_{\text{eff}} = 3(o_2)^2(\eta_2 - \epsilon_A o_2 + \tilde{J}_z s^2 o_2 - 2\tilde{J}_z s(\zeta - s)o_2). \quad (\text{B24})$$

From Eq. (B24) and the numerically determined CMFT wave functions we can calculate g_{eff} and thus predict the ground state in the degenerate region of CMFT from the sign of g_{eff} . The behavior of g_{eff} and $\text{sign}(g_{\text{eff}})$ over the relevant region of parameter space is shown in Fig. 11.

- [1] X.-G. Wen, *Phys. Rev. B* **65**, 165113 (2002).
- [2] L. Savary and L. Balents, *Rep. Prog. Phys.* **80**, 016502 (2017).
- [3] A. Kitaev, *Ann. Phys. (NY)* **321**, 2 (2006).
- [4] M. Hermele, M. P. A. Fisher, and L. Balents, *Phys. Rev. B* **69**, 064404 (2004).
- [5] A. Banerjee, S. V. Isakov, K. Damle, and Y. B. Kim, *Phys. Rev. Lett.* **100**, 047208 (2008).
- [6] M. J. P. Gingras and P. A. McClarty, *Rep. Prog. Phys.* **77**, 056501 (2014).
- [7] E. K.-H. Lee, R. Schaffer, S. Bhattacharjee, and Y. B. Kim, *Phys. Rev. B* **89**, 045117 (2014).
- [8] W.-J. Hu, S.-S. Gong, W. Zhu, and D. N. Sheng, *Phys. Rev. B* **92**, 140403(R) (2015).
- [9] Y. Iqbal, W.-J. Hu, R. Thomale, D. Poilblanc, and F. Becca, *Phys. Rev. B* **93**, 144411 (2016).
- [10] S. Depenbrock, I. P. McCulloch, and U. Schollwöck, *Phys. Rev. Lett.* **109**, 067201 (2012).
- [11] Y.-C. He, M. P. Zaletel, M. Oshikawa, and F. Pollmann, *Phys. Rev. X* **7**, 031020 (2017).
- [12] Y. Okamoto, M. Nohara, H. Aruga-Katori, and H. Takagi, *Phys. Rev. Lett.* **99**, 137207 (2007).
- [13] A. Banerjee, C. A. Bridges, J.-Q. Yan, A. A. Aczel, L. Li, M. B. Stone, G. E. Granroth, M. D. Lumsden, Y. Yiu, J. Knolle, S. Bhattacharjee, D. L. Kovrizhin, R. Moessner, D. A. Tennant, D. G. Mandrus, and S. E. Nagler, *Nat. Mater.* **15**, 733 (2016).
- [14] C. Balz, B. Lake, J. Reuther, H. Luetkens, R. Schonemann, T. Herrmannsdorfer, Y. Singh, A. T. M. Nazmul Islam, E. M. Wheeler, J. A. Rodriguez-Rivera, T. Guidi, G. G. Simeoni, C. Baines, and H. Ryll, *Nat. Phys.* **12**, 942 (2016).
- [15] M. R. Norman, *Rev. Mod. Phys.* **88**, 041002 (2016).
- [16] R. Sibille, N. Gauthier, H. Yan, M. Ciomaga Hatnean, J. Ollivier, B. Winn, U. Filges, G. Balakrishnan, M. Kenzelmann, N. Shannon, and T. Fennell, *Nat. Phys.* **14**, 711 (2018).
- [17] L.-J. Chang, S. Onoda, Y. Su, Y.-J. Kao, K.-D. Tsuei, Y. Yasui, K. Kakurai, and M. R. Lees, *Nat. Commun.* **3**, 992 (2012).
- [18] H. B. Cao, A. Banerjee, J.-Q. Yan, C. A. Bridges, M. D. Lumsden, D. G. Mandrus, D. A. Tennant, B. C. Chakoumakos, and S. E. Nagler, *Phys. Rev. B* **93**, 134423 (2016).
- [19] H. Takatsu, S. Onoda, S. Kittaka, A. Kasahara, Y. Kono, T. Sakakibara, Y. Kato, B. Fåk, J. Ollivier, J. W. Lynn, T. Taniguchi, M. Wakita, and H. Kadowaki, *Phys. Rev. Lett.* **116**, 217201 (2016).
- [20] E. Kermarrec, A. Zorko, F. Bert, R. H. Colman, B. Koteswararao, F. Bouquet, P. Bonville, A. Hillier, A. Amato, J. van Tol, A. Ozarowski, A. S. Wills, and P. Mendels, *Phys. Rev. B* **90**, 205103 (2014).
- [21] T.-H. Han, M. R. Norman, J.-J. Wen, J. A. Rodriguez-Rivera, J. S. Helton, C. Broholm, and Y. S. Lee, *Phys. Rev. B* **94**, 060409(R) (2016).
- [22] N. Martin, P. Bonville, E. Lhotel, S. Guitteny, A. Wildes, C. Decorse, M. Ciomaga Hatnean, G. Balakrishnan, I. Mirebeau, and S. Petit, *Phys. Rev. X* **7**, 041028 (2017).
- [23] Z. Zhu, P. A. Maksimov, S. R. White, and A. L. Chernyshev, *Phys. Rev. Lett.* **119**, 157201 (2017).
- [24] K. A. Ross, L. Savary, B. D. Gaulin, and L. Balents, *Phys. Rev. X* **1**, 021002 (2011).
- [25] Y.-D. Li, X. Wang, and G. Chen, *Phys. Rev. B* **94**, 035107 (2016).
- [26] K. Essafi, O. Benton, and L. D. C. Jaubert, *Phys. Rev. B* **96**, 205126 (2017).
- [27] R. Sibille, E. Lhotel, V. Pomjakushin, C. Baines, T. Fennell, and M. Kenzelmann, *Phys. Rev. Lett.* **115**, 097202 (2015).
- [28] R. Sibille, N. Gauthier, E. Lhotel, V. Porée, V. Pomjakushin, R. A. Ewings, T. G. Perring, J. Ollivier, A. Wildes, C. Ritter, T. C. Hansen, D. A. Keen, G. J. Nilsen, L. Keller, S. Petit, and T. Fennell, *Nat. Phys.* **16**, 546 (2020).
- [29] B. Gao, T. Chen, D. W. Tam, C.-L. Huang, K. Sasmal, D. T. Adroja, F. Ye, H. Cao, G. Sala, M. B. Stone, C. Baines, J. A. T. Verezhak, H. Hu, J.-H. Chung, X. Xu, S.-W. Cheong, M. Nallaiyan, S. Spagna, M. B. Maple, A. H. Nevidomskyy, E. Morosan, G. Chen, and P. Dai, *Nat. Phys.* **15**, 1052 (2019).
- [30] J. Gaudet, E. M. Smith, J. Dudemaine, J. Beare, C. R. C. Buhariwalla, N. P. Butch, M. B. Stone, A. I. Kolesnikov, G. Xu, D. R. Yahne, K. A. Ross, C. A. Marjerrison, J. D. Garrett, G. M. Luke, A. D. Bianchi, and B. D. Gaulin, *Phys. Rev. Lett.* **122**, 187201 (2019).
- [31] V. Peçanha-Antonio, E. Feng, X. Sun, D. Adroja, H. C. Walker, A. S. Gibbs, F. Orlandi, Y. Su, and T. Brückel, *Phys. Rev. B* **99**, 134415 (2019).
- [32] C. Mauws, A. M. Hallas, G. Sala, A. A. Aczel, P. M. Sarte, J. Gaudet, D. Ziat, J. A. Quilliam, J. A. Lussier, M. Bieringer, H. D. Zhou, A. Wildes, M. B. Stone, D. Abernathy, G. M. Luke, B. D. Gaulin, and C. R. Wiebe, *Phys. Rev. B* **98**, 100401(R) (2018).
- [33] S. Singh, S. Saha, S. K. Dhar, R. Suryanarayanan, A. K. Sood, and A. Revcolevschi, *Phys. Rev. B* **77**, 054408 (2008).
- [34] B. Z. Malkin, T. T. A. Lummen, P. H. M. van Loosdrecht, G. Dhalenne, and A. R. Zakirov, *J. Phys.: Condens. Matter* **22**, 276003 (2010).
- [35] J. Xu, Magnetic properties of rare-earth zirconate pyrochlores, Ph.D. thesis, Technischen Universität, Berlin, 2017.
- [36] E. Lhotel, S. Petit, S. Guitteny, O. Florea, M. Ciomaga Hatnean, C. Colin, E. Ressouche, M. R. Lees, and G. Balakrishnan, *Phys. Rev. Lett.* **115**, 197202 (2015).
- [37] J. Xu, V. K. Anand, A. K. Bera, M. Frontzek, D. L. Abernathy, N. Casati, K. Siemensmeyer, and B. Lake, *Phys. Rev. B* **92**, 224430 (2015).
- [38] S. Petit, E. Lhotel, B. Canals, M. Ciomaga Hatnean, J. Ollivier, H. Mutka, E. Ressouche, A. R. Wildes, M. R. Lees, and G. Balakrishnan, *Nat. Phys.* **12**, 746 (2016).
- [39] J. Xu, O. Benton, V. K. Anand, A. T. M. N. Islam, T. Guidi, G. Ehlers, E. Feng, Y. Su, A. Sakai, P. Gegenwart, and B. Lake, *Phys. Rev. B* **99**, 144420 (2019).
- [40] V. K. Anand, D. L. Abernathy, D. T. Adroja, A. D. Hillier, P. K. Biswas, and B. Lake, *Phys. Rev. B* **95**, 224420 (2017).
- [41] A. Bertin, P. Dalmas de Réotier, B. Fåk, C. Marin, A. Yaouanc, A. Forget, D. Sheptyakov, B. Frick, C. Ritter, A. Amato, C. Baines, and P. J. C. King, *Phys. Rev. B* **92**, 144423 (2015).
- [42] P. Dalmas de Réotier, A. Yaouanc, A. Maisuradze, A. Bertin, P. J. Baker, A. D. Hillier, and A. Forget, *Phys. Rev. B* **95**, 134420 (2017).
- [43] A. M. Hallas, A. M. Arevalo-Lopez, A. Z. Sharma, T. Munsie, J. P. Attfield, C. R. Wiebe, and G. M. Luke, *Phys. Rev. B* **91**, 104417 (2015).
- [44] D. Swarnakar, Y. Jana, J. Alam, and S. Nandi, *Phys. B: Condens. Matter* **521**, 93 (2017).
- [45] Y.-P. Huang, G. Chen, and M. Hermele, *Phys. Rev. Lett.* **112**, 167203 (2014).
- [46] J. G. Rau and M. J. Gingras, *Annu. Rev. Condens. Matter Phys.* **10**, 357 (2019).

- [47] O. Benton, O. Sikora, and N. Shannon, *Phys. Rev. B* **86**, 075154 (2012).
- [48] O. Benton, *Phys. Rev. B* **94**, 104430 (2016).
- [49] N. Shannon, O. Sikora, F. Pollmann, K. Penc, and P. Fulde, *Phys. Rev. Lett.* **108**, 067204 (2012).
- [50] L. Savary and L. Balents, *Phys. Rev. Lett.* **108**, 037202 (2012).
- [51] S.-B. Lee, S. Onoda, and L. Balents, *Phys. Rev. B* **86**, 104412 (2012).
- [52] O. Benton, L. D. C. Jaubert, R. R. P. Singh, J. Oitmaa, and N. Shannon, *Phys. Rev. Lett.* **121**, 067201 (2018).
- [53] Y. Kato and S. Onoda, *Phys. Rev. Lett.* **115**, 077202 (2015).
- [54] C.-J. Huang, Y. Deng, Y. Wan, and Z. Y. Meng, *Phys. Rev. Lett.* **120**, 167202 (2018).
- [55] C.-J. Huang, C. Liu, Z. Meng, Y. Yu, Y. Deng, and G. Chen, [arXiv:1806.04014](https://arxiv.org/abs/1806.04014).
- [56] Y.-D. Li and G. Chen, *Phys. Rev. B* **95**, 041106(R) (2017).
- [57] X. P. Yao, Y.-D. Li, and G. Chen, *Phys. Rev. Res.* **2**, 013334 (2020).
- [58] J. Chaloupka, G. Jackeli, and G. Khaliullin, *Phys. Rev. Lett.* **105**, 027204 (2010).
- [59] D. S. Rokhsar and S. A. Kivelson, *Phys. Rev. Lett.* **61**, 2376 (1988).
- [60] J. Xu, O. Benton, A. T. M. N. Islam, T. Guidi, G. Ehlers, and B. Lake, *Phys. Rev. Lett.* **124**, 097203 (2020).
- [61] A. S. Patri, M. Hosoi, and Y. B. Kim, *Phys. Rev. Res.* **2**, 023253 (2020).